Food Science of Animal Products

Research Article

Rapid pathogen discrimination on eggshells via hyperspectral imaging

Chengkang Liu[1], Yanbin Chen[1], Mengyuan Gu[1], Dongqiao Wang[2], Qiaohua Wang[1] ✉

[1] *College of Engineering, Huazhong Agricultural University, Wuhan 430070, China*
[2] *School of Mechanical Science and Engineering, Huazhong University of Science and Technology, Wuhan 430074, China*
✉Address correspondence to Qiaohua Wang, wqh@mail.hzau.edu.cn
Received: March 23, 2026; Revised: April 29, 2026; Accepted: July 21, 2026

Abstract: Eggshell surfaces are highly susceptible to *Escherichia coli* and *Salmonella enteritidis*, demanding rapid, non-destructive detection. This study evaluated hyperspectral imaging (HSI) for pathogen discrimination. Visible-near-infrared (Vis-NIR) and short-wave infrared systems acquired data from eggs contaminated at 10^3–10^5 CFU/mL. Raw Vis-NIR spectra with competitive adaptive reweighted sampling provided optimal features. The pathogens showed opposite reflectance trends, attributed to biofilm structural differences affecting light scattering and absorption. Classification models achieved up to 91.11% accuracy in pathogen identification and 88.89% accuracy in differentiating *E. coli* levels. Vis-NIR-HSI shows great potential for rapid, non-destructive eggshell pathogen detection, with a clarified mechanistic framework.

Keywords: hyperspectral imaging; egg safety; foodborne pathogen; non-destructive detection; spectral mechanism

Citation: C. K. Liu, Y. B. Chen, M. Y. Gu, et al., Rapid pathogen discrimination on eggshells via hyperspectral imaging, Food Sci. Anim. Prod. 4 (2026) 9240180. https://doi.org/10.26599/FSAP.2026.9240180.

1 Introduction

Eggs hold a significant position in the global diet as a nutritionally balanced food; however, their surfaces are highly vulnerable to environmental contamination by foodborne pathogens, particularly Gram-negative bacteria such as *Escherichia coli* and *Salmonella enteritidis*[1]. These pathogens possess strong survival and transmission capabilities during production, storage, and sale, constituting a major risk for bacterial foodborne illnesses[2–3]. While current detection relies on traditional plate counting or polymerase chain reaction (PCR), these methods are hindered by long cycles (24–48 h) and destructive sampling, which fail to meet the industry's demand for high-throughput, real-time, and non-destructive detection[4]. Thus, developing rapid techniques to identify specific pathogens and contamination levels without damaging samples is critical for food safety assurance.

Hyperspectral imaging (HSI), which integrates imaging and spectral analysis, has demonstrated significant advantages in food safety by providing a "spectral fingerprint" reflecting chemical composition, molecular structure, and surface micro-characteristics[5–7]. Previous research has confirmed HSI's effectiveness in pesticide residue detection, meat freshness assessment, and grain mold identification[8–9], as well as egg-specific applications like crack detection and freshness evaluation[10–11]. However, most existing egg-related HSI studies have been limited to identifying macroscopic physical defects (e.g., cracks, dirt) or quantifying overall spoilage via total bacterial load, often treating microbial contamination as a generic variable. This leaves a critical gap in advancing the technology from general contamination monitoring to species-specific pathogen discrimination. Furthermore, achieving this discrimination at early or low contamination levels remains a formidable challenge. At low levels of contamination (e.g., < 10^4 CFU/eggshell), early-stage biofilms are structurally sparse and optically thin. Their weak spectral signatures are easily obscured by the complex natural optical variations of the eggshell surface. Therefore, determining whether HSI can be pushed to its sensitivity limits to capture these subtle, pathogen-specific signals prior to massive biofilm formation is highly necessary for early food safety warnings.

From a microscopic perspective, pathogen attachment on eggshells is closely linked to biofilm formation—complex structures encased in extracellular polymeric substances (EPS) that enhance resistance to environmental stressors[12]. Due to differences in cell wall structure, metabolic activity, and biofilm capacity, different pathogens induce distinct physicochemical changes during attachment, such as alterations in surface hydration, light scattering, and molecular vibration patterns[13–14]. These changes manifest as unique spectral features, offering an optical basis for differentiation. However, previous HSI applications in food microbiology often rely on purely data-driven "black-box" models, lacking a fundamental explanation of the physical origin of the spectral signals. Correlating HSI data with the physicochemical properties of specific biofilms and uncovering the underlying optical-biological mechanisms (such as the competition between light scattering and absorption driven by biofilm architecture) remains a key challenge to be addressed in order to transition HSI from an empirical tool to a theoretically grounded analytical method.

Based on this, the present study systematically evaluates the feasibility of HSI for eggshell pathogen detection with a clear hierarchy of goals. The primary objective is to develop a robust methodological framework for species-specific pathogen discrimination and to elucidate the underlying spectral-biofilm response mechanisms. The secondary objective is to extend this framework to evaluate its capability for quantitative contamination-level assessment, thereby exploring its translational potential for industrial risk-grading applications. To achieve these goals, the research is structured around four specific tasks: 1) acquiring visible-near-infrared (Vis-NIR) and short-wave infrared (SWIR) spectral data at different contamination levels and evaluating

© Beijing Academy of Food Sciences 2026. Food Science of Animal Products published by Tsinghua University Press. This is an open access article under the CC BY-NC-ND license (http://creativecommons.org/licenses/by-nc-nd/4.0/).

preprocessing efficacy; 2) employing variable selection algorithms to screen key wavelengths associated with specific pathogens; 3) constructing and comparing machine and deep learning models for the non-destructive identification of contamination types and levels; and 4) exploring the physicochemical basis of spectral differences by combining spectral features with biofilm characteristics. This research aims to provide a comprehensive analytical framework for rapid, non-destructive pathogen discrimination on eggshells, promoting HSI's application in food microbial safety.

2 Materials and methods

2.1 Samples and bacterial strains

Fresh eggs (n = 150) were purchased from a commercial poultry farm. To prevent spectral variations associated with shelf-life degradation and internal moisture loss, eggs were collected within 24 h of oviposition and temporarily stored at 4 °C. All eggs were screened to ensure intact shells[15]. To ensure strict sterile baseline conditions, the eggs were surface-wiped with 75% ethanol, exposed to ultraviolet (UV) light for 15 min, and sealed in sterile bags until use. Two typical foodborne pathogens, *E. coli* (strain LZ5) and *S. enteritidis* (strain Sal10116), were used in this study. These strains were selected based on their high detection rates in egg contamination and public health significance[16]. These specific strains were originally isolated from the intestinal contents of experimentally challenged laying hens and confirmed via 16S rRNA sequencing by the College of Animal Science and Technology, Huazhong Agricultural University, which provided them for this research. Prior to use, the provided *E. coli* strain was inoculated into a liquid medium (composition: 10 g tryptone, 5 g yeast extract, 10 g NaCl, 1 000 mL distilled water, pH 7.0 ± 0.2) and activated in a constant temperature incubator at 37 °C for 24 h. Similarly, the *S. enteritidis* strain was inoculated into a liquid medium (composition: 10 g tryptone, 16.5 g brain heart infusion powder, 5 g NaCl, 2.5 g Na_2HPO_4, 2 g glucose, 1 000 mL distilled water, pH 7.4 ± 0.2) and activated at 37 °C for 24 h.

2.2 Simulated contamination and sample preparation

To simulate early-stage contamination during washing, transportation, or contact with contaminated water, a whole-egg immersion method was employed for sample preparation[17]. The sterile physiological saline used for dilution consisted purely of 0.85 g/100 mL NaCl in distilled water, completely free of organic components to avoid any spectral baseline interference. The activated *E. coli* and *S. enteritidis* suspensions were serially diluted to 10^3, 10^4, and 10^5 CFU/mL using this sterile saline. The eggs were assigned to three groups: *E. coli* group (n = 60), *S. enteritidis* group (n = 60), and control group (n = 30). Each pathogen group was further subdivided into three concentration gradients, with 20 eggs per gradient (n = 20). The eggs were immersed in the respective bacterial suspensions for 5 min. The control group was immersed in sterile physiological saline for 5 min. Following immersion, all eggs were removed and allowed to air-dry naturally under sterile conditions for 60 min to promote initial biofilm attachment. To verify the actual surface contamination levels, standard plate counting was performed on randomly selected samples after the drying phase. The entire eggshell surface was thoroughly swabbed using sterile cotton swabs moistened with sterile saline. The swabbed suspensions were serially diluted, spread onto agar plates, and incubated at 37 °C for 24 h. The bacterial load was calculated and expressed as lg (CFU/eggshell).

2.3 HSI system and acquisition conditions

To capture molecular and structural information across different spectral ranges, two push-broom HSI systems were used[18]: a Vis-NIR system (391–1 043 nm, 520 bands) and a SWIR system (869–1 770 nm, 512 bands). Each system was equipped with a translation stage and uniformly illuminated halogen light sources. The angle between the light source and lens was fixed at 45° to minimize specular reflection. The sample-to-lens distance was set to 50 cm for the Vis-NIR system and 40 cm for the SWIR system. The spectral resolution was 0.5 nm/pixel, and the spatial resolution was 0.25 mm/pixel. All acquisitions were conducted at room temperature ((25 ± 2) °C) under constant humidity ((50 ± 5)%).

To eliminate the effects of sensor dark current and uneven illumination, white and black reference corrections were performed before sample scanning. White reference: a polytetrafluoroethylene standard white board (reflectance > 99%); black reference: signal obtained with the lens completely covered. After correction, the sample reflectance (R) was calculated using the formula (1):

$$R = \frac{R_I - R_D}{R_W - R_D} \quad (1)$$

Where R_I is the raw sample image, and R_D and R_W are the black and white reference images, respectively.

The resulting spectral reflectance data were used for subsequent analysis[19].

2.4 Spectral data preprocessing and analysis pipeline

2.4.1 Spectral data extraction and preprocessing

For each eggshell sample, a rigorous segmentation procedure was implemented to define the region of interest (ROI). First, a binary mask was generated using image thresholding to separate the entire eggshell from the dark background. To minimize spectral distortions caused by edge curvature, the ROI was restricted to the central rectangular area of the egg surface. Within this central area, pixels exhibiting specular reflection (glare) or dark anomalies (e.g., natural micro-stains) were systematically excluded based on reflectance intensity thresholds. Then, spectral data from all valid pixels within the ROI were extracted, and their average spectrum was calculated as the representative spectrum for that sample. To improve the signal-to-noise ratio and enhance spectral features related to biochemical components, eight preprocessing methods (including a baseline control) were systematically compared[20]: 1) no preprocessing (No Prep) was used as a baseline control to evaluate the classification potential of the raw spectra; 2) multiplicative scatter correction (MSC) and standard normal variate (SNV) transformation were used to minimize light scattering effects caused by uneven particle distribution; 3) mean centering (MC) was applied to adjust the spectral baseline for improved model convergence; 4) first derivative (FD) processing aimed to highlight subtle spectral variations; 5) standardization (STD) and Min-Max normalization (M-M) mapped spectral data to a uniform numerical range to reduce the impact of scale differences on models; 6) Savitzky-Golay smoothing (SG) was employed to effectively suppress random noise while preserving the original spectral shape. All preprocessing operations were implemented in a Python environment using the scikit-learn and NumPy libraries.

2.4.2 Feature wavelength selection

To establish a spectral feature subset highly correlated with pathogen type and contamination level, three variable selection

algorithms were employed to screen key wavelengths: 1) the competitive adaptive reweighted sampling (CARS) algorithm combined exponential decay and adaptive weighted sampling, using partial least square regression coefficients as weights to select wavelengths significant for classification; 2) the successive projections algorithm (SPA) used a forward selection strategy to sequentially construct wavelength combinations, eliminating wavelengths with high collinearity and redundancy through projection analysis; 3) the uninformative variable elimination (UVE) method introduced random noise variables as a reference and eliminated wavelength bands contributing no meaningful information to the model based on stability assessment. This process not only reduced data dimensionality but also laid the foundation for constructing a spectro-biological marker system with clear chemical interpretability[21].

2.4.3 Classification model construction

To comprehensively evaluate the classification potential of the spectral data, a multi-model parallel analysis strategy was adopted, encompassing the following models: traditional machine learning models (*K*-nearest neighbors (KNN), support vector machine (SVM), and random forest (RF)) and deep learning models (one-dimensional convolutional neural network (1D-CNN) and Transformer encoder).

During model training, five-fold cross-validation (CV) combined with grid search was used for hyperparameter optimization of traditional machine learning models. For deep learning models, an independent validation set was used to monitor the training process, and an early stopping strategy was employed to prevent overfitting.

2.4.4 Model performance evaluation

To prevent overfitting and ensure an unbiased assessment, the dataset was randomly partitioned into a training set (75%) and an independent test set (25%). Model hyperparameter optimization was conducted exclusively on the training set via five-fold CV combined with grid search. Crucially, the final performance of all classifiers (KNN, SVM, RF, 1D-CNN, and Transformer), preprocessing techniques, and feature selection algorithms was evaluated strictly on the unseen independent test set.

Model performance was primarily evaluated using classification accuracy. Because the dataset was strictly balanced across all pathogen types and concentration gradients, overall accuracy serves as an unbiased primary metric. In addition, detailed confusion matrices were generated to provide a comprehensive, class-wise breakdown of misclassifications for the grading tasks. Furthermore, to objectively compare and select the optimal preprocessing and feature selection methods, a unified comprehensive scoring system was established. This system evaluated each method based on the performance of all classifiers (KNN, SVM, RF, 1D-CNN, Transformer) across three dimensions: average accuracy (the mean accuracy of all classifiers on the test set (A_{test}); weight: 0.2), CV accuracy (the mean accuracy of all classifiers during CV (A_{CV}); weight: 0.4), stability metric (a robustness measure calculated based on the standard deviation of accuracies (M_{sta}), which was linealy normalized into the range of 1–100; weight: 0.4). The final composite score was calculated using the weighted formula (2):

$$\text{Composite score}\ (\%) = 0.2 \times A_{test} + 0.4 \times A_{CV} + 0.4 \times M_{sta} \quad (2)$$

All data analysis and model implementation were completed in a Python 3.8 environment, primarily relying on open-source libraries such as scikit-learn (version 1.3.2), PyTorch (version 2.0.1), and SciPy (version 1.10.1).

3 Results and discussion

3.1 Surface bacterial load and biofilm formation characteristics

To verify the controllability and authenticity of the simulated contamination, total colony counts were determined for egg samples inoculated at different concentrations (10^3–10^5 CFU/mL). As shown in Table 1, the surface loads of both *E. coli* and *S. enteritidis* increased significantly with higher inoculation concentrations, rising from approximately 2 to 4 (lg (CFU/eggshell)), indicating that the whole-egg immersion method successfully simulated a realistic contamination state ranging from mild to severe[22].

Notably, at the same inoculation concentration, the *E. coli* load was generally higher than that of *S. enteritidis*, with the exception of the 10^4 CFU/mL group where the loads were virtually identical (3.28 *vs.* 3.30 (lg (CFU/eggshell))). Despite this exception, the overall trend remained. For example, at 10^3 CFU/mL, the average value for the *E. coli* group was 2.37 (lg (CFU/eggshell)), compared to 2.11 (lg (CFU/eggshell)) for the *S. enteritidis* group, showing a slight but consistent difference. This phenomenon is closely related to the biofilm formation characteristics of the two strains[23]. Literature reports indicated that *E. coli* can secrete abundant EPS, forming a dense and hydrophobic biofilm structure that enhances its adhesion to hydrophobic surfaces like the eggshell cuticle[24]. In contrast, the biofilm of *S. enteritidis* is thinner and more susceptible to environmental stresses (e.g., desiccation)[25], leading to lower survival rates during the drying phase. This difference suggests that the variations in surface attachment and biofilm formation mechanisms between the two pathogens may be the intrinsic source of their spectral response specificity[26].

Table 1 Statistical analysis of bacterial counts on eggshell surfaces.

Group	Inoculum (CFU/mL)	Range (lg (CFU/eggshell))	Mean (lg (CFU/eggshell))	SD (lg (CFU/eggshell))
E. coli	10^3	1.59–2.80	2.37	0.26
	10^4	2.45–3.74	3.28	0.36
	10^5	4.08–4.61	4.39	0.14
S. enteritidis	10^3	1.74–2.51	2.11	0.21
	10^4	2.63–3.70	3.30	0.29
	10^5	4.08–4.46	4.32	0.12
Control	nd	nd	nd	nd

Note: SD, standard deviation; nd, not detected.

3.2 Pathogen-specific spectral response mechanism

3.2.1 Spectral fingerprint features in the Vis-NIR band

Figure 1 shows the average reflectance spectra and SD bands for the three sample groups in the 391–1 043 nm. Signals in the Vis region (391–760 nm) were significantly influenced by the eggshell's natural pigments (e.g., protoporphyrin IX absorption peaks at 589 and 643 nm) and surface texture, resulting in wider error bands[27]. In the NIR region (760–1 043 nm), the reflectance curves became smoother, signal stability improved, providing an optimal detection window for contamination feature identification[28].

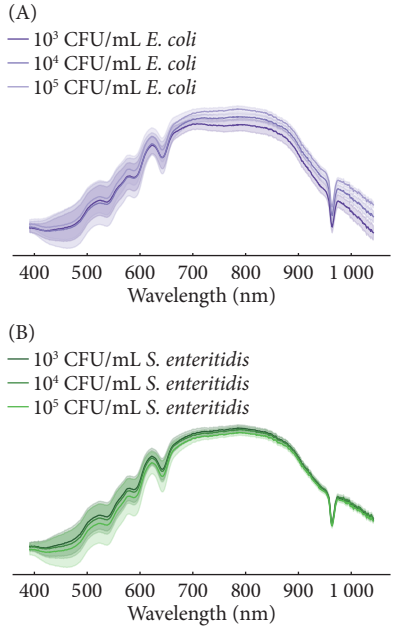

Figure 1 Average reflectance spectra and SD bands for samples at different contamination levels of (A) *E. coli* and (B) *S. enteritidis* in the Vis-NIR spectral ranges.

Most crucially, the two pathogens exhibited contrasting reflectance trends: as the contamination level increased, the overall reflectance of the *E. coli* group increased, while that of the *S. enteritidis* group decreased. This opposite trend indicates that optical property changes caused by different contamination types can be effectively captured by HSI. Based on the observed spectral phenomena and well-documented microbiological literature, we hypothesize that the possible mechanisms include: 1) enhanced scattering effect: *E. coli* biofilm are generally reported to be thicker and looser in structure, increasing surface roughness and leading to multiple scattering of incident light, thereby raising reflectance; 2) enhanced absorption effect: *S. enteritidis* biofilm are typically described as denser and has a higher hydration state, leading to stronger absorption by O–H and N–H bonds, thereby lowering reflectance.

At the molecular level, the feature near 872 nm is related to the third overtone of N–H stretching vibrations in proteins and cell wall structures[29]; the absorption peaks near 760, 960, and 980 nm are primarily attributed to O–H stretching vibrations of water[30]. The directional differences in reflectance changes at these wavelengths for the two bacteria further support the hypothesis that differences in biofilm hydration capacity lead to spectral feature divergence.

3.2.2 Spectral feature analysis in the SWIR band

Within the 869–1 770 nm range, spectral differences among sample groups were relatively weaker (Figure 2). This band primarily reflects molecular vibration information related to proteins (N–H vibrations, 1 020–1 510 nm), lipids (C–H second overtone, 940–1 200 nm), and water (O–H absorption, 1 596 nm)[31]. These features are less sensitive to subtle surface structural changes compared to the Vis-NIR region. Therefore, the SWIR band is more suitable for characterizing overall chemical composition rather than specific surface contamination differences. This result verifies the superior advantage of the Vis-NIR band in identifying micro-physical changes associated with early biofilm formation.

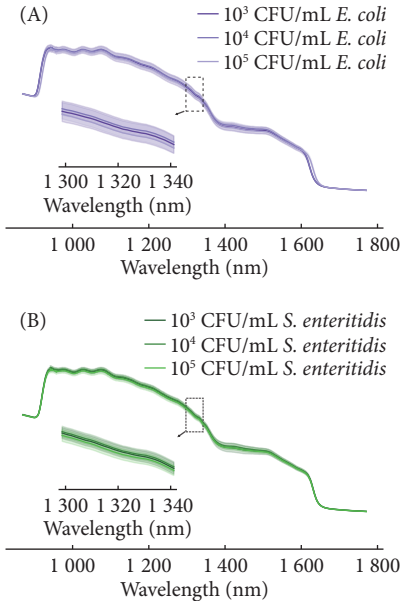

Figure 2 Average reflectance spectra and SD bands for samples at different contamination levels of (A) *E. coli* and (B) *S. enteritidis* in the SWIR spectral ranges.

3.3 Pathogen discrimination based on spectral biomarkers

To construct a high-precision, interpretable spectral identification model for pathogens, this study first determined the optimal preprocessing strategies for the Vis-NIR and SWIR bands. Subsequently, the most robust feature wavelength selection algorithms for each band were screened through comprehensive performance metrics. Finally, the intrinsic relationship between spectral signals and bacterial load was validated by analyzing the model's discrimination patterns for contamination levels.

3.3.1 Comparison of preprocessing effects and determination of optimal methods

To establish a high-precision, high-robustness pathogen discrimination model, eight spectral preprocessing methods were systematically evaluated for their performance in the Vis-NIR (391–1 043 nm) and SWIR (869–1 770 nm) bands. Based on the test set accuracy of five classifiers (KNN, SVM, RF, 1D-CNN, Transformer) and the comprehensive scoring system, the optimal preprocessing strategy for each band was determined.

In the Vis-NIR band, different preprocessing methods significantly impacted model performance (Figure 3A). The SVM achieved perfect classification accuracy (100%) with No Prep,

demonstrating its ability to capture subtle feature differences in raw spectra. RF also reached 100% accuracy after FD processing, and KNN achieved excellent performance (95.56%) under the same preprocessing. This indicates that FD processing can effectively enhance subtle spectral variations related to biofilm physical structure, thereby improving the performance of models relying on decision boundaries or distance metrics (e.g., RF and KNN). Deep learning models (1D-CNN and Transformer) performed poorly in this band, with the highest accuracy being only 48.89%. Moreover, they were extremely sensitive to preprocessing like standardization, with accuracy plummeting to near zero.

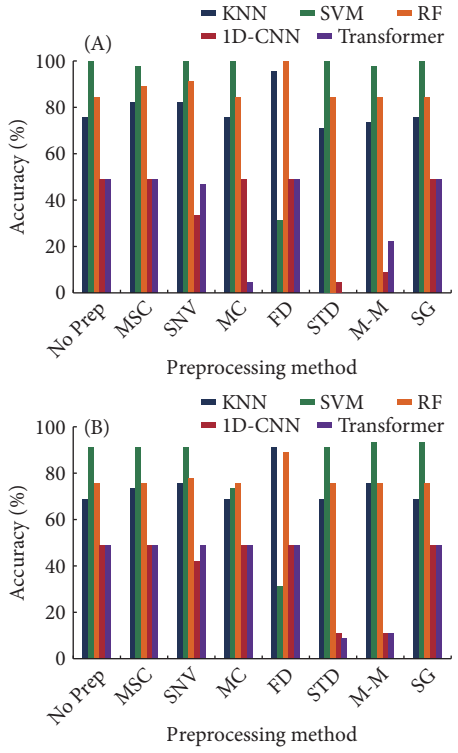

Figure 3 Classification accuracy of different preprocessing methods combined with various models in the (A) Vis-NIR and (B) SWIR spectral ranges.

Based on the composite score (Figure 4A), No Prep was rated the optimal preprocessing strategy for the Vis-NIR band with a composite score of 68.39%. Its advantage lies in fully preserving the overall reflectance changes and baseline differences caused by biofilm surface scattering effects in the raw spectra. This information is crucial for distinguishing the inherent optical properties of *E. coli* (reflectance increases with contamination) and *S. enteritidis* (reflectance decreases with contamination).

In the SWIR band, the overall model accuracy was lower than in the Vis-NIR band, and the optimal preprocessing method changed (Figure 3B). SVM achieved the highest single-model accuracy in this band (93.3%) after M-M. The best performances for both KNN and RF occurred after FD preprocessing, with accuracies of 91.11% and 88.89%, respectively. Deep learning models still did not achieve ideal results in this band.

Composite scoring results (Figure 4B) showed that MC became the best preprocessing method for the SWIR band with a composite score of 66.28%, closely followed by SNV and MSC. These methods enhance the model's discrimination capability and stability by eliminating baseline drift or scattering effects, thereby highlighting absorption peak features related to chemical components like proteins and lipids (e.g., lipid C–H bonds near 1 200 nm, protein N–H bonds near 1 510 nm).

The different preprocessing requirements for the two bands reflect the underlying differences in their dominant optical mechanisms: the discrimination power in the Vis-NIR band primarily stems from light scattering effects caused by differences in the macroscopic physical structure (e.g., thickness, roughness) of pathogen biofilms. Therefore, the No Prep strategy, which retains the original reflectance signal, is most effective. The discrimination information in the SWIR band is more embedded in molecular vibration absorptions related to the chemical composition of biofilms (e.g., water, proteins, lipids). Therefore, methods like MC and SNV are needed to suppress physical interference and enhance spectral features related to chemical composition.

In summary, this study determined No Prep for the Vis-NIR band and MC for the SWIR band as the standardized preprocessing workflow for subsequent feature wavelength selection and modeling. This choice is based not only on the quantitative

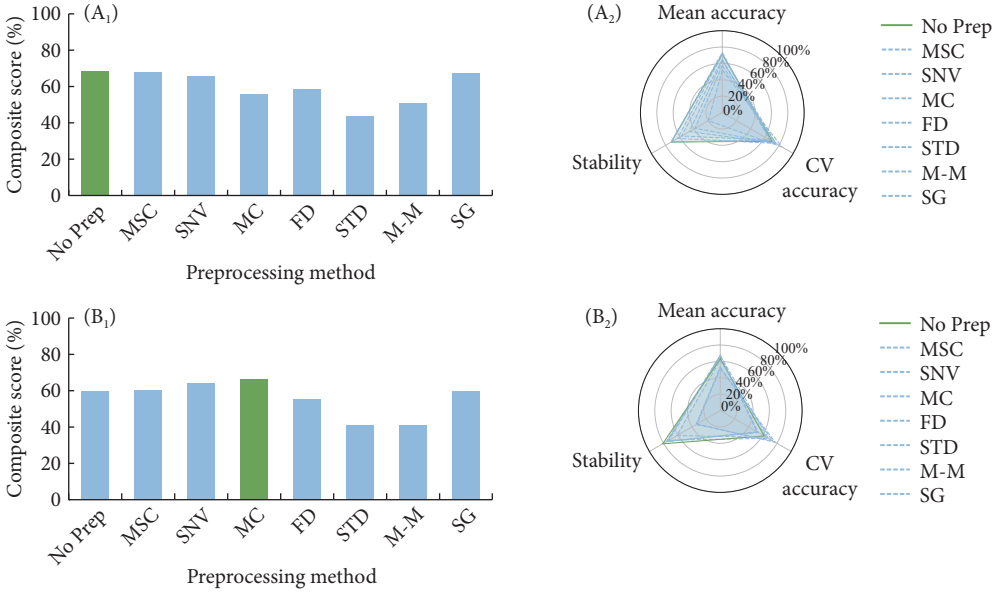

Figure 4 Composite scores of different preprocessing methods for the (A_1 and A_2) Vis-NIR and (B_1 and B_2) SWIR spectral ranges.

evaluation of model performance but also strongly supported by the mechanism of spectral-biofilm interaction.

3.3.2 *Feature wavelength selection and variable optimization*

Based on the determined optimal preprocessing methods (Vis-NIR: No Prep; SWIR: MC), three feature selection algorithms (CARS, SPA, UVE) were employed to reduce the dimensionality of the high-dimensional spectral data, aiming to build a classification model with high accuracy, strong robustness, and clear physical meaning. The goal of this study was to find a robust and portable detection solution. Therefore, a comprehensive scoring system was used for evaluation, which, while considering average accuracy, placed more emphasis on CV performance (weight: 0.4) and inter-model stability (weight: 0.4) to screen for a universal feature set insensitive to model selection and with strong generalization ability. The results indicated that the optimal feature selection strategy was significantly band-dependent, and its mechanism was closely related to the optical nature of the bands.

In the Vis-NIR band, combinations of different feature selection methods and classifiers showed diverse performance. From the perspective of the best performance of a single model (Table 2), the combination of the Transformer model and the SPA algorithm achieved the highest test accuracy (93.33%) in this band, demonstrating the advantage of combining cutting-edge architecture with efficient feature selection. However, this "peak performance" comes with a high risk of model dependency. The SPA method aims to construct a variable combination with minimal redundancy through forward selection, but this highly optimized combination may overfit the internal representation of complex models like Transformer, resulting in an extremely low stability index (3.08%). This means that once the model architecture changes, its performance may fluctuate significantly, indicating insufficient robustness.

From the perspective of the comprehensive scoring system (Figure 5A), the CARS method ranked first with a composite score of 50.15%. Its advantage lies in providing a common feature foundation with good and stable performance for all five types of

Table 2 Accuracy (%) of classification models built with different feature selection methods on the training and test sets for both spectral ranges.

Model	Feature selection method	Vis-NIR		SWIR	
		Training set	Test set	Training set	Test set
KNN	CARS	72.12	71.11	72.12	68.89
	SPA	72.12	68.89	72.12	64.44
	UVE	68.27	62.22	70.19	66.67
SVM	CARS	76.92	71.11	74.04	68.89
	SPA	77.88	71.11	74.04	66.67
	UVE	71.15	68.89	74.04	68.89
RF	CARS	78.85	71.11	75.00	71.11
	SPA	86.54	73.33	80.77	62.22
	UVE	86.54	75.56	77.88	71.11
1D-CNN	CARS	65.38	66.67	72.12	75.56
	SPA	63.46	66.67	70.19	73.33
	UVE	77.88	82.22	71.15	73.33
Transformer	CARS	88.46	91.11	84.62	75.56
	SPA	97.12	93.33	92.31	84.44
	UVE	94.23	91.11	68.27	71.11

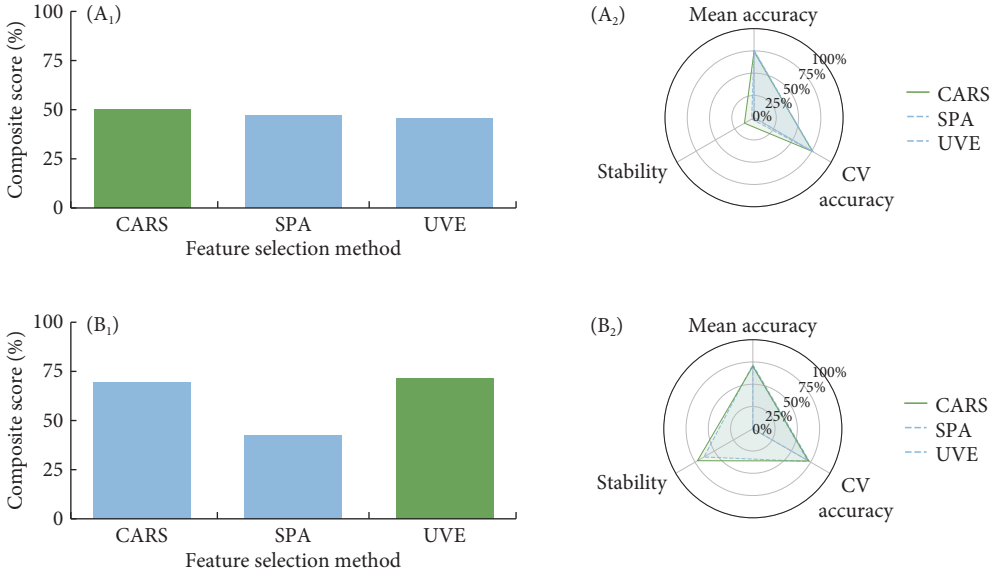

Figure 5 Composite scores of different feature selection algorithms for the (A_1 and A_2) Vis-NIR and (B_1 and B_2) SWIR spectral ranges.

models. Its good CV accuracy (75.85%) and best stability index (12.42%) indicate that the feature set screened by CARS has stronger generalization ability. The underlying mechanism is as follows: spectral differences in the Vis-NIR band are primarily dominated by light scattering effects caused by differences in the physical structure of pathogen biofilms. The CARS algorithm dynamically retains a set of wavelength variables most significant for classification through adaptive reweighted sampling and exponential decay forces. This process simulates a "survival of the fittest" natural selection, and the finally selected feature wavelengths (Figure 6A) can comprehensively and balancedly reflect the overall scattering characteristics of the biofilm[32]. Therefore, the CARS feature set contains richer physical discriminant information, enabling models of varying complexity, from simple to complex, to learn effectively from it. This achieves "model-inclusive" high performance, which is the fundamental reason for its superior composite score.

In the SWIR band, as shown in Table 2 and Figure 5B, the UVE method achieved an overwhelmingly high composite score (71.66%). Its advantage stems from an extremely high stability index (68.78%) and good CV accuracy (72.27%). Although its average test accuracy (70.22%) was not the highest, it had the lowest SD (2.27%). This indicates that the feature wavelength combination screened by UVE can provide a consistent and reliable performance benchmark for various models, demonstrating unparalleled robustness. In stark contrast, the SPA method performed poorly in this band, as shown in Figure 5B, with the lowest composite score (42.35%) and a stability index of 0, again exposing its high sensitivity to model selection in the SWIR band. The mechanism of this phenomenon is as follows: spectral information in the SWIR band mainly originates from molecular bond vibration absorptions of biofilm chemical components (e.g., proteins, lipids, water). These absorption peaks are distinct and stable, but collinearity between features may be strong. The core idea of the UVE algorithm is to use randomly generated noise variables as a "reference system" and ruthlessly eliminate original wavelength variables that contribute weakly or unstably to the model based on stability assessment[33]. This method is particularly suitable for the SWIR band because it can effectively screen out "core" absorption feature bands with high signal-to-noise ratio, strong correlation with chemical components, and stable contribution from the complex absorption background (Figure 6B). The resulting spectral biomarker set has clear physicochemical meaning and is insensitive to the model algorithm, thus providing a pure and robust feature input for all classifiers.

In summary, based on the robustness requirements for practical application, the optimal feature selection scheme for different bands was determined. This choice is not only data-driven but also deeply determined by the combined effect of the optical mechanism of the bands and the inherent principles of the feature selection algorithms. For the Vis-NIR band, the CARS algorithm is recommended. Its adaptive competition mechanism can effectively capture scattering features, which are relatively widespread and dominated by biofilm physical structure, achieving the best balance between accuracy and stability. For the SWIR band, the UVE algorithm is recommended. Its noise reference filtering mechanism can efficiently lock absorption features that are clear, stable, and dominated by chemical composition, thereby providing the most robust discrimination capability.

3.3.3 Validation analysis of the correlation between spectral response and bacterial load

During model construction, a key observation emerged: feature selection does not universally improve classification performance; its utility is highly dependent on the specific "model-band" combination. A comprehensive analysis of this phenomenon is crucial for avoiding over-optimization and establishing an efficient technical pathway. Furthermore, extending the model's capability from qualitative pathogen discrimination to quantitative bacterial load assessment (10^3, 10^4, 10^5 CFU/mL) is essential for practical food safety warnings. To deeply explore the intrinsic link between hyperspectral signals and bacterial surface load, the model's response capabilities to different contamination levels were systematically analyzed through the following aspects:

1) Algorithm-dependent mechanisms of feature selection. Comparative data revealed that the internal mechanisms of different algorithms dictate their response to high-dimensional data. For traditional machine learning models (e.g., KNN and RF), utilizing preprocessing alone occasionally yielded superior results.

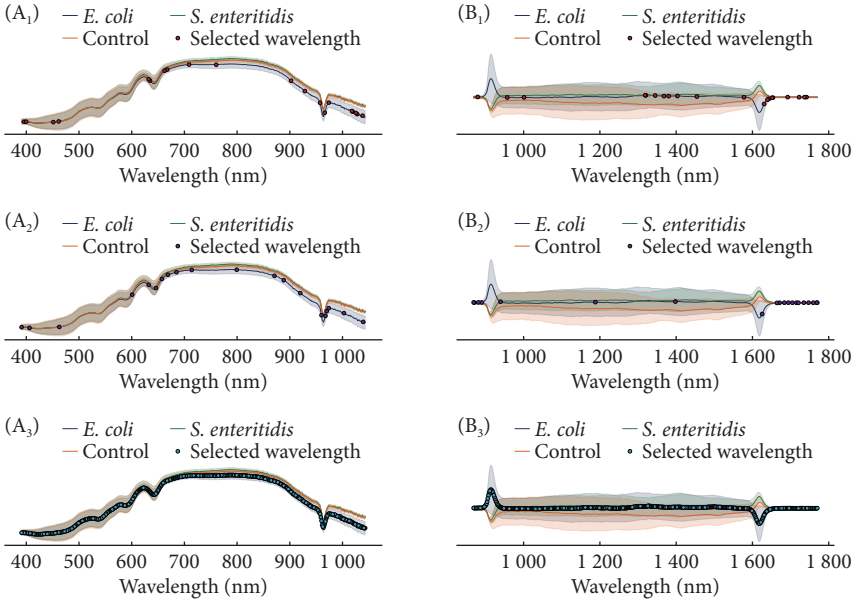

Figure 6 Distribution of key wavelengths selected by different feature selection algorithm in the (A) Vis-NIR and (B) SWIR spectral range. (A_1 and B_1) CARS; (A_2 and B_2) SPA; (A_3 and B_3) UVE.

For instance, in the Vis-NIR band, RF and KNN achieved highly accurate species discrimination using only FD processing without external feature selection. The underlying mechanism is that FD processing greatly enhances subtle spectral variations, while tree-based models and distance metrics inherently possess feature-weighting capabilities. In these cases, retaining the full spectral data provides a complete "feature candidate pool", whereas an additional feature selection step might prematurely eliminate wavelengths with synergistic discriminant effects. Conversely, deep learning models (e.g., Transformer and 1D-CNN) exhibited a substantial performance leap when combined with feature selection (e.g., Transformer accuracy surged from 48.89% to 91.11% with CARS (Figure 3)). Due to their massive parameter space, deep learning models are highly susceptible to the "curse of dimensionality" and background noise. Here, feature selection acts as a critical "pre-dimensionality reducer". It is important to note that the total sample size in this study (150 samples) is relatively limited for training highly complex architectures like the Transformer from scratch. This limited sample size, relative to the vast parameter space of the models, fundamentally explains their poor and unstable performance on the raw, high-dimensional spectra. Feature selection effectively alleviated this data-hunger by providing a pure, low-redundancy input. Furthermore, while the limited sample size could introduce variance, the robust 5-fold CV employed during training ensured that the reported performances were not the result of a lucky random seed, but represented a stable learning outcome on the optimized feature sets.

2) Quantitative evaluation relying solely on preprocessing. To evaluate whether the full-spectrum intensity systematically correlates with bacterial load, models utilizing only preprocessing (the concise pathway) were first tested. Under the FD-KNN combination for the Vis-NIR band, the model achieved a 77.78% test accuracy for grading *E. coli* contamination levels, but performed poorly for *S. enteritidis* (only 38.89% accuracy, as shown in Table 3).

Similarly, in the SWIR band, the concise FD-RF combination yielded inadequate accuracies for both *E. coli* (61.11%) and *S. enteritidis* (66.67%) load quantification (Table 4). These results indicate that while full-spectrum preprocessing is sufficient for identifying broader bacterial species, it lacks the sensitivity required to robustly capture the subtle, concentration-dependent spectral patterns induced by varying bacterial loads.

3) Quantitative evaluation based on the standardized feature-engineered pathway. Guided by the multi-metric evaluation framework, the standardized pathway (preprocessing + feature selection + model) was thoroughly evaluated for load quantification. In the Vis-NIR band, the optimal No Prep-CARS-Transformer combination achieved an impressive 88.89% accuracy in differentiating *E. coli* contamination levels (Table 5).

Crucially, the Vis-NIR confusion matrix (Figure 7A) revealed that the model perfectly identified the lowest (10^3 CFU/mL) and highest (10^5 CFU/mL) *E. coli* levels with 100% accuracy and zero false negatives. Minor misclassifications only occurred at the

Table 3 Model accuracy (%) for the combination of FD and KNN algorithm within the Vis-NIR spectral ranges.

Model	Preprocessing method	Feature selection method	*E. coli*		*S. enteritidis*	
			Training set	Test set	Training set	Test set
KNN	FD	–	92.86	77.78	57.14	38.89

Note: –, without external feature selection.

Table 4 Model accuracy (%) for the combination of FD and RF algorithm within the SWIR spectral ranges.

Model	Preprocessing method	Feature selection method	*E. coli*		*S. enteritidis*	
			Training set	Test set	Training set	Test set
RF	FD	–	88.10	61.11	85.71	66.67

Note: –, without external feature selection.

Table 5 Model accuracy (%) for the combination of No Prep and CARS-Transformer within the Vis-NIR spectral ranges.

Model	Preprocessing method	Feature selection method	*E. coli*		*S. enteritidis*	
			Training set	Test set	Training set	Test set
Transformer	No Prep	CARS	88.10	88.89	76.19	55.56

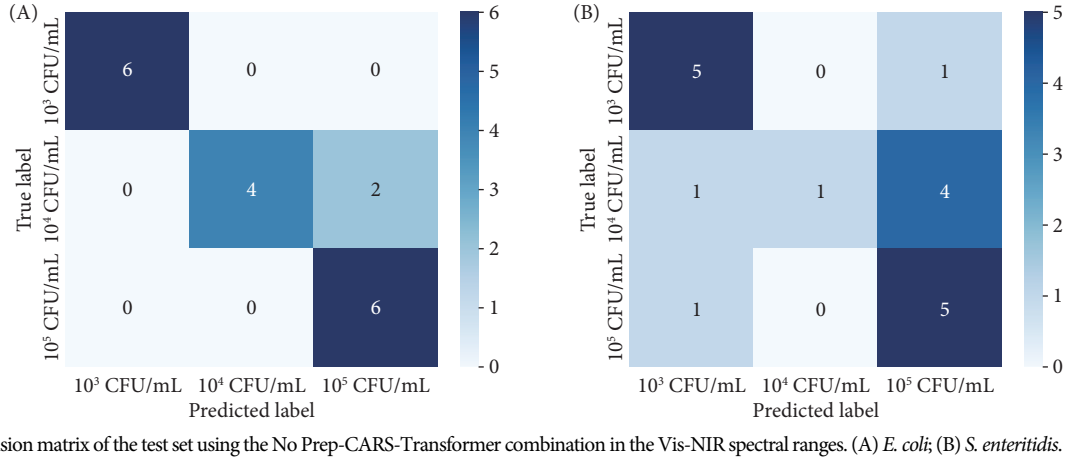

Figure 7 Confusion matrix of the test set using the No Prep-CARS-Transformer combination in the Vis-NIR spectral ranges. (A) *E. coli*; (B) *S. enteritidis*.

medium concentration (10^4 CFU/mL). Although the accuracy for *S. enteritidis* (Figure 7B) was lower due to similar overlap at the medium level, its ability to correctly flag high-risk samples remained robust, making this pathway highly effective for early safety warnings.

In contrast, the optimal SWIR combination (MC-UVE-1D-CNN) achieved 66.67% and 61.11% test accuracy for differentiating *E. coli* and *S. enteritidis* contamination levels, respectively (Table 6).

The SWIR confusion matrices displayed severe cross-level misclassifications (Figure 8). For instance, low-level *E. coli* (10^3 CFU/mL) was predominantly misidentified as medium-level (Figure 8A), while high-level *S. enteritidis* (10^5 CFU/mL) was frequently underestimated as lower levels (Figure 8B). This pervasive confusion confirms the inherent physical limitation of the SWIR band: its shallow penetration depth and water absorption saturation make it fundamentally unsuitable for precise quantitative surface load assessment.

In summary, the transition from simple preprocessing to a standardized feature-engineering framework is highly justified. The No Prep-CARS-Transformer pathway for the Vis-NIR band effectively captures the subtle physical scattering changes associated with biofilm growth, achieving high-precision, robust grading of *E. coli* contamination levels. In contrast, the SWIR band confirmed physically-rooted limitations in quantitative contamination assessment, rendering it more suitable for qualitative species discrimination. Therefore, the standardized feature-engineered pathway provides a reliable methodological basis for transitioning HSI technology from laboratory discrimination to online, intelligent food safety grading.

3.4 Chemical mechanisms of spectral-biofilm interaction

The differences in hyperspectral response are rooted in the distinct physicochemical properties of the two pathogens' biofilms, leading to their differential impact on light scattering and absorption behavior.

3.4.1 Structure-dominated differences in optical response

We hypothesize that the differences in hyperspectral response are rooted in the distinct physicochemical properties of the two pathogens' biofilm structures. Literature indicates that *E. coli* tends to form thicker, looser biofilms. Their abundant EPS form a porous network, increasing surface roughness and light scattering capacity, leading to increased reflectance in the Vis-NIR region. In contrast, *S. enteritidis* biofilms are typically thinner, denser, and have a higher hydration state. This structure promotes internal light absorption (especially in O–H and N–H related bands), resulting in decreased reflectance. Therefore, the competition mechanism between light scattering and absorption is the core physical basis explaining the spectral response differences between the two types of pathogens.

3.4.2 Chemical basis of molecular vibration fingerprints

At the molecular level, spectral differences can be traced back to changes in the vibration patterns of hydrogen-containing functional groups. In the Vis-NIR band, features around 760, 960, and 980 nm are closely related to water O–H bonds, while features around 872 nm are related to N–H bonds in proteins. Differences in water content, EPS composition, and density between the two biofilms directly alter the abundance and microenvironment of these key functional groups, thereby modulating absorption intensity at specific wavelengths. The correlation between reflectance changes and contamination levels observed in this study's data confirms that spectral features can sensitively reflect the dynamic evolution of biofilm chemical composition.

3.4.3 Proposal of a multi-scale mechanistic model

In summary, this study proposes a multi-scale mechanistic framework to explain spectral-biofilm interactions: at the microscopic scale, the specific chemical composition (type and abundance of functional groups) of the biofilm determines the intrinsic absorption characteristics; at the mesoscopic scale, the physical structure of the biofilm (porosity, density, thickness) regulates the light scattering path and absorption efficiency; at the macroscopic scale, the combined effects of the above factors ultimately manifest as the specific reflectance spectrum captured by HSI. This framework links spectral response to microbial surface colonization behavior, not only providing a theoretical explanation

Table 6 Model accuracy (%) for the combination of MC-UVE and 1D-CNN algorithm within the SWIR spectral ranges.

Model	Preprocessing method	Feature selection method	*E. coli*		*S. enteritidis*	
			Training set	Test set	Training set	Test set
1D-CNN	MC	UVE	73.81	66.67	57.14	61.11

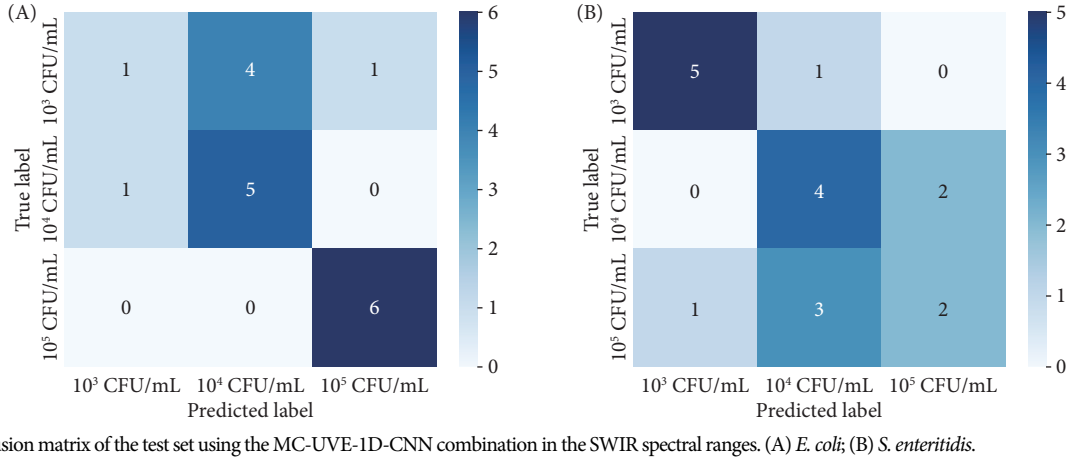

Figure 8 Confusion matrix of the test set using the MC-UVE-1D-CNN combination in the SWIR spectral ranges. (A) *E. coli*; (B) *S. enteritidis*.

for hyperspectral discrimination but also indicating that this technology can serve as a powerful tool for probing microbe-interface interactions.

4 Industrial application and relevance

4.1 Current industrial practices and unmet needs

In commercial egg processing plants, microbiological safety of table eggs is typically monitored using conventional culture-based methods and, to a lesser extent, PCR or immunoassays. These approaches are generally applied on a batch or sampling basis and require 24–48 h to deliver results, during which eggs have usually already entered downstream packaging and distribution. Moreover, most of these methods are destructive and cannot be used for 100% inspection of individual eggs on fast-moving grading lines. As a result, early-stage shell contamination by pathogens such as *E. coli* and *S. enteritidis* may remain undetected, and contaminated batches can only be identified retrospectively through surveillance data or consumer complaints, leading to high economic and reputational costs.

4.2 Integration of the proposed HSI system into egg grading lines

The Vis-NIR HSI system and modelling framework developed in this study are well suited for integration into modern egg grading and packing lines. A typical high-throughput line handles 10 000–12 000 eggs per hour, corresponding to approximately 170–200 eggs per minute on each conveyor lane. In our configuration, a push-broom Vis–NIR HSI unit (391–1 043 nm) can acquire a full-shell spectrum image of a single egg within approximately 0.2 s under controlled illumination. When combined with a synchronized conveyor and line-scan triggering, this acquisition speed is compatible with industrial line speeds and allows single-file, egg-by-egg inspection without interrupting the existing grading workflow.

For practical implementation, the HSI module can be positioned downstream of washing and drying but upstream of weight grading and visual inspection. At this stage, the shell surface is relatively clean and dry, minimizing interference from free water and gross dirt and thus improving the reliability of spectral measurements. The proposed configuration requires only a compact camera enclosure, uniform halogen or light-emitting diode line lights, a simple mechanical mounting frame, and an industrial computer, and can be retrofitted into existing lines with minimal modification to the plant layout.

However, the widespread industrial adoption of HSI is often constrained by the high cost of full-spectrum cameras and the need to handle large hyperspectral datasets. In this context, the present study provides an important optimization pathway. Our CARS-based feature selection in the Vis-NIR range demonstrated that a small number of characteristic wavelengths, especially those around 760, 872, and 960 nm that are associated with biofilm hydration and light scattering, already contain sufficient discriminatory information for accurate pathogen detection. This finding suggests that equipment manufacturers could develop customized, low-cost multispectral sensors that acquire only these key bands, instead of the full continuous spectrum. Such application-specific multispectral devices would substantially reduce hardware investment and computational load for real-time processing, while preserving the high classification accuracy achieved by the full HSI system. Therefore, the proposed integration scheme is not limited to laboratory-grade hyperspectral cameras, but also points to a scalable, cost-effective sensor design tailored for industrial egg grading lines.

4.3 Real-time pathogen screening and risk grading strategy

The best-performing Vis-NIR-based workflow identified in this work—using raw spectra combined with CARS-selected features and a Transformer classifier—achieved 91.11% accuracy in discriminating *E. coli* from *S. enteritidis* and 88.89% accuracy in differentiating three *E. coli* contamination levels (10^3, 10^4, 10^5 CFU/mL). These performance metrics enable a practically useful risk-grading strategy for online monitoring.

In an industrial scenario, model outputs can be mapped to three operational categories: 1) “Pass”: eggs predicted to be free from target pathogens or at very low contamination levels enter normal grading and packaging; 2) “Require treatment”: eggs predicted to have medium contamination levels are diverted to enhanced decontamination steps, such as intensified washing or additional disinfection; and 3) “Reject”: eggs predicted to carry high contamination levels (corresponding to 10^5 CFU/mL in our experiments) are automatically removed from the line and recorded for trace-back investigation. Given that the full pipeline from image acquisition to model decision can be completed within a fraction of a second, this risk-grading strategy can be implemented in real time without reducing line throughput.

4.4 Economic and operational feasibility

Although a full life-cycle cost analysis is beyond the scope of this study, a preliminary assessment suggests that the proposed HSI-based system is economically and operationally feasible. The capital expenditure for a single-lane Vis-NIR HSI module, including camera, optics, illumination, mechanical mounting, and industrial computer, is comparable to that of existing machine vision systems commonly installed for crack or dirt detection. Once installed, the system operates automatically and can be integrated with the plant’s programmable logic controller to control diverters, alarms, and data logging, thereby adding microbiological screening capability without increasing manual workload.

From a cost-benefit perspective, even a modest reduction in the incidence or size of microbiological recalls can offset the investment. For large producers handling tens of thousands of eggs per day, a single recall event can incur direct product losses and indirect costs (logistics, testing, brand damage) far exceeding the cost of installing an online inspection module. In contrast, continuous, non-destructive screening of all eggshells enables early interception of high-risk batches and provides objective documentation of process control, which may also support compliance with increasingly stringent regulatory and customer audits.

4.5 Practical challenges and roadmap for industrial deployment

Several practical challenges must be addressed before full-scale industrial deployment. First, eggshells vary widely in colour (e.g., white *vs.* brown) and surface texture, which can introduce baseline shifts and scattering differences in the spectra. Second, industrial environments are subject to fluctuations in ambient temperature, vibration, and stray light, all of which may affect spectral stability

and model robustness. Third, the spectral models developed here were trained under controlled laboratory conditions and need to be further validated on multi-batch, multi-farm datasets to ensure generalizability.

These challenges can be mitigated through a stepwise implementation roadmap. In the short term, pilot-scale trials can be conducted on semi-industrial test lines, where the current models are evaluated and incrementally updated using transfer learning to cover different shell colours, production lots, and environmental conditions. In parallel, standardized calibration procedures (using white/black references and stable check samples) can be established for daily verification of system performance. In the longer term, building a shared spectral-microbiological database across different plants would enable more robust, plant-independent models and support the development of industry-wide guidelines for hyperspectral pathogen screening on eggshells.

5 Conclusions

This study systematically elucidated the effectiveness of HSI technology for discriminating foodborne pathogens on eggshells and its underlying mechanisms. The core conclusions are as follows:

A pathogen-specific spectral response mechanism based on biofilm structural differences was revealed. In the Vis-NIR band, contamination by *E. coli* and *S. enteritidis* led to opposite reflectance evolution trends. This is directly attributed to the different optical effects (enhanced scattering for the former, enhanced absorption for the latter) triggered by differences in the density and hydration state of their respective biofilms. This band was significantly superior to the SWIR band in capturing such surface micro-physical changes.

A robust feature extraction and modeling framework was established. The study determined that using raw spectral data combined with the CARS algorithm was the optimal strategy for extracting stable discriminant features from Vis-NIR data. Models built on this basis not only achieved high-precision identification of the two pathogens (highest test accuracy 91.11%) but also demonstrated good ability to differentiate *E. coli* contamination levels (test accuracy 88.89%), confirming its potential for quantitative assessment.

Support was provided for non-destructive detection technology development, spanning from methodology to theory. The research findings clarify the technical pathway for using Vis-NIR HSI for the rapid, non-destructive discrimination of pathogens on eggshells. The proposed multi-scale correlation mechanism between spectral response and biofilm characteristics not only deepens the understanding of the detection principle but also lays a methodological and theoretical foundation for extending this technology to microbial safety monitoring of other food substrates. Despite these promising results, the current study has certain limitations. First, the proposed multi-scale mechanistic model is primarily inferred from spectral data and existing literature. Future research should integrate direct microscopic and biochemical characterizations (e.g., scanning electron microscopy and EPS quantification) to provide direct physical evidence for these spectral-biofilm interactions. Second, the current study is limited to strictly controlled laboratory conditions and specific egg types. Future research should focus on validating and updating the proposed models across diverse eggshell colors and textures, as well as optimizing the system's robustness for complex, multi-batch industrial environments.

Conflict of interest

The authors declared that they have no conflict of interest.

Acknowledgments

This research was funded by National Key R&D Program of China (2022YFD1300400), National Natural Science Foundation of China (32372426) and National Key R&D Program of China (2024YFD2000901).

Author contributions

Chengkang Liu: Conceptualization, methodology, software, writing-original draft preparation; Yanbin Chen: Data curation; Mengyuan Gu: Visualization, investigation; Dongqiao Wang: Supervision; Qiaohua Wang: Validation, writing-reviewing and editing.

Data availability

The authors declare that the data supporting the findings of this study are available from the corresponding author upon reasonable request.

References

[1] D. Solís, N. Cordero, M. Quezada-Reyes, et al., Prevalence of *Salmonella* in eggs from conventional and cage-free egg production systems and the role of consumers in reducing household contamination, Foods 12(23) (2023) 4300. https://doi.org/10.3390/foods12234300.

[2] A. G. Abdelhamid, A. E. Yousef, Egg-associated *Salmonella enterica* serovar Enteritidis: comparative genomics unveils phylogenetic links, virulence potential, and antimicrobial resistance traits, Front. Microbiol. 14 (2023) 1278821. https://doi.org/10.3389/fmicb.2023.1278821.

[3] K. K. Chousalkar, P. Flynn, M. Sutherland, et al., Recovery of *Salmonella* and *Escherichia coli* from commercial egg shells and effect of translucency on bacterial penetration in eggs, Int. J. Food Microbiol. 142(1/2) (2010) 207–213. https://doi.org/10.1016/j.ijfoodmicro.2010.06.029.

[4] E. M. Atwa, S. Xu, A. K. Rashwan, et al., Advances in emerging non-destructive technologies for detecting raw egg freshness: a comprehensive review, Foods 13(22) (2024) 3563. https://doi.org/10.3390/foods13223563.

[5] D. Patel, S. Bhise, S. S. Kapdi, et al., Non-destructive hyperspectral imaging technology to assess the quality and safety of food: a review, Food Prod. Process. Nutr. 6(1) (2024) 69. https://doi.org/10.1186/s43014-024-00246-4.

[6] J. H. So, S. Y. Joe, S. H. Hwang, et al., Current advances in detection of abnormal egg: a review, J. Anim. Sci. Technol. 64(5) (2022) 813. https://doi.org/10.5187/jast.2022.e56.

[7] R. Siche, R. Vejarano, V. Aredo, et al., Evaluation of food quality and safety with hyperspectral imaging (HSI), Food Eng. Rev. 8(3) (2016) 306–322. https://doi.org/10.1007/s12393-015-9137-8.

[8] C. Xie, Y. He, External characteristic determination of eggs and cracked eggs identification using spectral signature, Sci. Rep. 6(1) (2016) 21130. https://doi.org/10.1038/srep21130.

[9] D. Liu, X. A. Zeng, D. W. Sun, et al., Recent developments and applications of hyperspectral imaging for quality evaluation of agricultural products: a review, Crit. Rev. Food Sci. Nutr. 55(12) (2015) 1744–1757. https://doi.org/10.1080/10408398.2014.981743.

[10] Y. Z. Feng, D. W. Sun, Application of hyperspectral imaging in food safety inspection and control: a review, Crit. Rev. Food Sci.

Nutr. 52(11) (2012) 1039–1058. https://doi.org/10.1080/10408398.2011.584403.

[11] D. P. Smith, K. C. Lawrence, G. W. Heitschmidt, et al., Detection of hatching and table egg defects using hyperspectral imaging, in European Poultry Conference Proceedings (2006).

[12] S. Shaji, R. K. Selvaraj, R. Shanmugasundaram, et al., *Salmonella* infection in poultry: a review on the pathogen and control strategies, Microorganisms 11(11) (2023) 2814. https://doi.org/10.3390/microorganisms11112814.

[13] I. Gantois, R. Ducatelle, F. Pasmans, et al., Mechanisms of egg contamination by *Salmonella* Enteritidis, FEMS Microbiol. Rev. 33(4) (2009) 718–738. https://doi.org/10.1111/j.1574-6976.2008.00161.x.

[14] M. S. Kapena, J. B. Muma, C. M. Mubita, et al., Antimicrobial resistance of *Escherichia coli* and *Salmonella* in raw retail table eggs in Lusaka, Zambia, Vet. World 13(11) (2020) 2528. https://doi.org/10.14202/vetworld.2020.2528-2533.

[15] K. de Reu, K. Grijspeerdt, W. Messens, et al., Eggshell factors influencing eggshell penetration and whole egg contamination by different bacteria, including *Salmonella* Enteritidis, Int. J. Food Microbiol. 112(3) (2006) 253–260. https://doi.org/10.1016/j.ijfoodmicro.2006.04.011.

[16] T. J. Humphrey, Contamination of egg shell and contents with *Salmonella* Enteritidis: a review, Int. J. Food Microbiol. 21(1/2) (1994) 31–40. https://doi.org/10.1016/0168-1605(94)90197-X.

[17] B. Y. Mahmoud, D. A. Semida, S. S. Elnesr, et al., Approaches of egg decontamination for sustainable food safety, Sustainability 15(1) (2022) 464. https://doi.org/10.3390/su15010464.

[18] Y. Lu, Y. Huang, R. Lu, Innovative hyperspectral imaging-based techniques for quality evaluation of fruits and vegetables: a review, Appl. Sci. 7(2) (2017) 189. https://doi.org/10.3390/app7020189.

[19] M. Nikzadfar, M. Rashvand, H. Zhang, et al., Hyperspectral imaging aiding artificial intelligence: a reliable approach for food qualification and safety, Appl. Sci. 14(21) (2024) 9821. https://doi.org/10.3390/app14219821.

[20] M. Rogers, J. Blanc-Talon, M. Urschler, et al., Wavelength and texture feature selection for hyperspectral imaging: a systematic literature review, J. Food Meas. Charact. 17(6) (2023) 6039–6064. https://doi.org/10.1007/s11694-023-02044-x.

[21] Q. Dai, J. H. Cheng, D. W. Sun, et al., Advances in feature selection methods for hyperspectral image processing in food industry applications: a review, Crit. Rev. Food Sci. Nutr. 55(10) (2015) 1368–1382. https://doi.org/10.1080/10408398.2013.871692.

[22] C. Carrascosa, D. Raheem, F. Ramos, et al., Microbial biofilms in the food industry: a comprehensive review, Int. J. Environ. Res. Public Health 18(4) (2021) 2014. https://doi.org/10.3390/ijerph18042014.

[23] A. Bridier, P. Sanchez-Vizuete, M. Guilbaud, et al., Biofilm-associated persistence of food-borne pathogens, Food Microbiol. 45 (2015) 167–178. https://doi.org/10.1016/j.fm.2014.04.015.

[24] S. Galie, C. García-Gutiérrez, E. M. Miguélez, et al., Biofilms in the food industry: health aspects and control methods, Front. Microbiol. 9 (2018) 898. https://doi.org/10.3389/fmicb.2018.00898.

[25] C. Milho, M. D. Silva, D. Alves, et al., *Escherichia coli* and *Salmonella* Enteritidis dual-species biofilms: interspecies interactions and antibiofilm efficacy of phages, Sci. Rep. 9(1) (2019) 18183. https://doi.org/10.1038/s41598-019-54847-y.

[26] X. Zhao, F. Zhao, J. Wang, et al., Biofilm formation and control strategies of foodborne pathogens: food safety perspectives, RSC Adv. 7(58) (2017) 36670–36683. https://doi.org/10.1039/C7RA02497E.

[27] D. Wu, D. W. Sun, Advanced applications of hyperspectral imaging technology for food quality and safety analysis and assessment: a review—Part I: fundamentals, Innov. Food Sci. Emerg. Technol. 19 (2013) 1–14. https://doi.org/10.1016/j.ifset.2013.04.014.

[28] K. Yao, J. Sun, J. Cheng, et al., Development of simplified models for non-destructive hyperspectral imaging monitoring of *S*-ovalbumin content in eggs during storage, Foods 11(14) (2022) 2024. https://doi.org/10.3390/foods11142024.

[29] A. Lee, S. Park, J. Yoo, et al., Detecting bacterial biofilms using fluorescence hyperspectral imaging and various discriminant analyses, Sensors 21(6) (2021) 2213. https://doi.org/10.3390/s21062213.

[30] M. Kovar, M. Brestic, O. Sytar, et al., Evaluation of hyperspectral reflectance parameters to assess the leaf water content in soybean, Water 11(3) (2019) 443. https://doi.org/10.3390/w11030443.

[31] G. Mishra, B. K. Panda, W. A. Ramirez, et al., Application of SWIR hyperspectral imaging coupled with chemometrics for rapid and non-destructive prediction of aflatoxin B_1 in single kernel almonds, LWT-Food Sci. Technol. 155 (2022) 112954. https://doi.org/10.1016/j.lwt.2021.112954.

[32] W. Li, Y. Wu, L. Du, et al., Hyperspectral imaging for foreign matter detection in foods: advances, challenges, and future directions, Foods 14(17) (2025) 3026. https://doi.org/10.3390/foods14173026.

[33] Q. J. Han, H. L. Wu, C. B. Cai, et al., An ensemble of Monte Carlo uninformative variable elimination for wavelength selection, Anal. Chim. Acta 612(2) (2008) 121–125. https://doi.org/10.1016/j.aca.2008.02.032.